ChemComm

Chemical Communications

rsc.li/chemcomm

I found the synergistic active sites …

ROYAL SOCIETY
OF CHEMISTRY
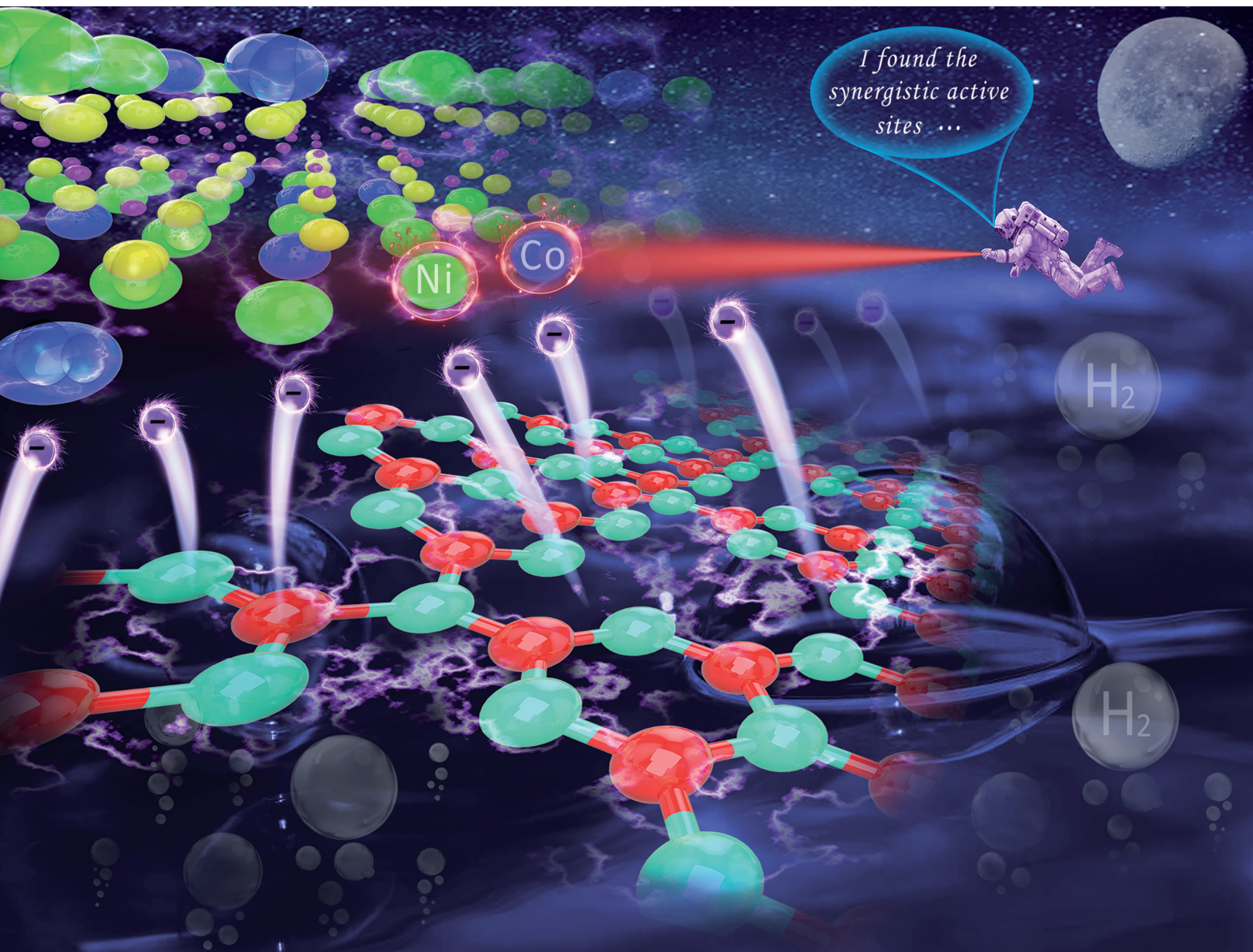
COMMUNICATION
Weikang Wang, Hua Tang, Qinqin Liu *et al.*
A 2D bimetallic Ni–Co hydroxide monolayer cocatalyst for
boosting photocatalytic H$_2$ evolution

Check for updates

A 2D bimetallic Ni–Co hydroxide monolayer cocatalyst for boosting photocatalytic H₂ evolution†

Haiwei Su,[a] Xiaohui Yu,[a] Weikang Wang, [iD] *[b] Lele Wang,[a] Hua Tang*[ac] and Qinqin Liu [iD] *[a]

Here, we report two-dimensional (2D) Ni–Co hydroxide monolayers (NiCo-HMs) as a highly active cocatalyst for enhancing the photocatalytic H₂ evolution of 2D g-C₃N₄ nanosheets. The NiCo-HMs can expand the interface of electron migration, promote the separation of photogenerated carriers, provide synergistic Co–Ni active sites, and optimize atomic hydrogen adsorption to improve the kinetics of the catalytic reaction. The resulting 2D/2D NiCo-HMs/g-C₃N₄ heterojunction displays a high photocatalytic H₂ evolution of 3.58 mmol g⁻¹ h⁻¹.

Hydrogen (H₂) evolution through solar water splitting is an effective approach to provide renewable energy.[1–3] However, the photocatalytic H₂ evolution strongly depends on the separation efficiency of photogenerated carriers of semiconductors. To boost the carrier separation, employing appropriate cocatalysts in photocatalysis has been evidenced to be an efficient strategy.[4] Among various reported cocatalysts, the transition metal hydroxides (TMHs) with oxygen bridges and hydroxyl groups have started to show their brilliance due to their excellent charge transfer ability and abundant edge reaction active sites.[5–7] When compared with their mono-metallic counterparts, bimetallic hydroxides with the synergistic advantages of composed dual metals can supply multichannel carrier separation and optimized active sites to boost the kinetics of the catalytic reaction.[8–10]

Moreover, the TMHs always exhibit a typical two-dimensional (2D) layered structure.[11] Reducing the layer number of TMHs to a unique monolayer structure can expose more inner atoms as reaction active sites, and simultaneously the distance of photogenerated carrier migration from the internal migration surface would

be shortened to reduce the carrier quenching.[12,13] Furthermore, the 2D monolayer structure is also in favour of providing a reasonable platform to couple with semiconductors for developing efficient photocatalysts with reliable interface contact. Consequently, the bimetallic hydroxide monolayers are promising as cocatalysts to enhance the activity of the photocatalytic H₂ evolution reaction (HER).

Herein, a bimetallic nickel–cobalt hydroxide monolayer (NiCo-HM) as a cocatalyst was designed and *in situ* loaded on the protonated g-C₃N₄ nanosheets (PCN) to improve the photocatalytic H₂ evolution performance (Fig. S1a, ESI†). The zeta potentials of different samples under the condition of preparation process are illustrated in Fig. S1b (ESI†). It is noted that a strong interfacial connection can be formed in the interface between NiCo-HMs and PCN with opposite zeta potentials, which is helpful for electron transfer, leading to improved HER performance.[14]

Since Ni atoms and Co atoms have the same atomic valence type and a similar atom radius (R) (R_{Ni} = 1.62 Å, R_{Co} = 1.67 Å), the Ni atom can replace the Co atom to form a solid solution with a surrogate structure during the preparation process. Fig. 1a illustrates the atom structure model of NiCo-HMs. As expected, the transmission electron microscopy (TEM) image (Fig. 1b) shows a thin lamellar morphology of NiCo-HMs. In addition, the atomic force microscopy (AFM) image illustrates that the height of NiCo-HMs is about 0.6 nm (Fig. 1c), evidencing its monolayer structure.[15] The crystalline structure of NiCo-HMs is further revealed using high-resolution transmission electron microscopy (HRTEM) (Fig. S2, ESI†) and selected area electron diffraction (SAED) images (Fig. S3, ESI†). The observed crystal lattices of NiCo-HMs are 0.219 and 0.373 nm, corresponding to the (002) and (103) planes, respectively. For the TEM images of the NiCo-HMs-3/PCN composites (Fig. 1d), the coexistence of polygonal NiCo-HM monolayers and irregular lamellar PCN nanosheets illustrates a 2D/2D configuration. Furthermore, a well-established interfacial contact between NiCo-HMs and PCN as well as two exposed surfaces of (002)

[a] School of Materials Science and Engineering, Jiangsu University, Zhenjiang, Jiangsu, 212013, P. R. China. E-mail: qqliu@ujs.edu.cn

[b] School of Environmental and Chemical Engineering, Jiangsu University of Science and Technology, Zhenjiang, Jiangsu, 212100, P. R. China

[c] School of Environmental Science and Engineering, Qingdao University, Qingdao, 266071, P. R. China
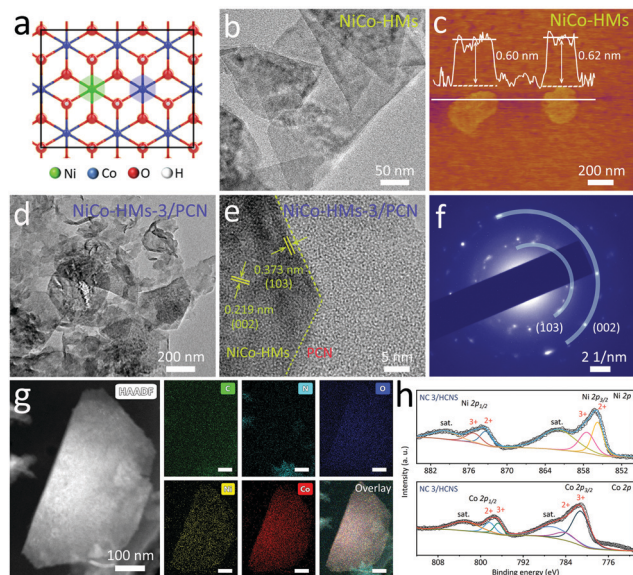
Fig. 1 (a) Structural model, (b) TEM image and (c) AFM image and corresponding height profile of monolayer NiCo-HMs. (d) TEM image, (e) HRTEM image and (f) SAED pattern of NiCo-HMs-3/PCN. (g) HAADF-STEM image and corresponding elemental mapping and (h) XPS high-resolution spectra of Ni 2p and Co 2p for NiCo-HMs-3/PCN.

and (103) planes belonging to the NiCo-HMs are observed in the TEM image (Fig. 1e) and the SAED pattern of the NiCo-HMs-3/PCN (Fig. 1f). The results indicate that the *in situ* growth of NiCo-HMs over PCN does not change the monolayer structure and exposed the crystal planes of the NiCo-HMs in the composite photocatalyst.

Moreover, the HAADF-STEM mapping images (Fig. 1g) show similar distribution shapes of Ni, Co and O elements, and demonstrate it to be a trapezoid nanosheet, indicating that the observed trapezoid nanosheet is NiCo-HMs. The elements of C and N are uniformly distributed over the NiCo-HM nanosheet, suggesting the successful fabrication of NiCo-HMs/PCN. The crystalline phase and structure of the as-prepared samples were analyzed using the X-ray diffraction (XRD) patterns (Fig. S4a, ESI†). The PCN shows two broad diffraction peaks at 27.3° and 13.1°, respectively. In contrast, NiCo-HMs exhibit a set of sharp and narrow peaks, assigned to β-Co(OH)$_2$ and β-Ni(OH). The diffraction peaks of the NiCo-HMs in the composite are similar but not the same as those of Ni(OH)$_2$ and Co(OH)$_2$, which means that the NiCo-HMs possess a solid-solution structure formed by Co and Ni atoms, similar to that of Ni(OH)$_2$ and Co(OH)$_2$. Clearly, both diffraction peaks belonging to the NiCo-HMs and PCN are found in the XRD patterns of the NiCo-HMs/PCN composites. Furthermore, an additional vibration mode attributed to the characteristics of the β-phase hydroxide is also observed at 3640 cm^{-1} in the FT-IR spectra of NiCo-HMs/PCN, Ni(OH)$_2$/PCN and Co(OH)$_2$/PCN (Fig. S4b, ESI†), revealing the successful growth of NiCo-HMs, Ni(OH)$_2$ and Co(OH)$_2$ over the PCN.

The X-ray photoelectron spectroscopy (XPS) full-spectrum and corresponding high-resolution spectra of C 1s, N 1s and

O 1s of NiCo-HMs-3/PCN are shown in Fig. S5 (ESI†). Fig. 1h illustrates the XPS high-resolution spectra of Ni 2p and Co 2p for NiCo-HMs-3/PCN. The Ni 2p spectrum can be deconvoluted into six peaks of Ni^{2+} and Ni^{3+} species, including two paired peaks and two shakeup satellites. Similarly, the Co 2p spectra are also assigned to the characteristic signals of Co^{2+} and Co^{3+} cations.[16] The specific value of these peaks and content information are presented in Table S1 (ESI†). The above experimental results indicated that various valences (2+ and 3+) of Co and Ni co-presented in the NiCo-HMs, providing rough evidence of the successful combination of NiCo-HMs over PCN to form the NiCo-HMs/PCN composite.

The photocatalytic activity of prepared samples was evaluated under a light-emitting diode (LED, 80 W) light source (Fig. S6, ESI†). As expected, the pristine PCN produced only traces of H$_2$ (Fig. 2a and b), while with NiCo-HMs as cocatalysts, the H$_2$ generation rate of NiCo-HMs/PCN significantly increased. The highest H$_2$ evolution rate of 3.58 mmol g^{-1} h^{-1} is achieved by NiCo-HMs-3/PCN. In addition, compared to mono-metallic hydroxide (0.66 and 1.70 mmol g^{-1} h^{-1} for Co(OH)$_2$/PCN and Ni(OH)$_2$/PCN), NiCo-HMs demonstrate a better cocatalytic effect for the photocatalytic HER (Fig. 2c and d). Furthermore, the H$_2$ generation of NiCo-HMs-3/PCN even exceeds that of the Pt nanoparticle (NP) loaded PCN (1% Pt$_{NP}$/PCN, Fig. S7, ESI†). A brief literature comparison of the photocatalytic HER
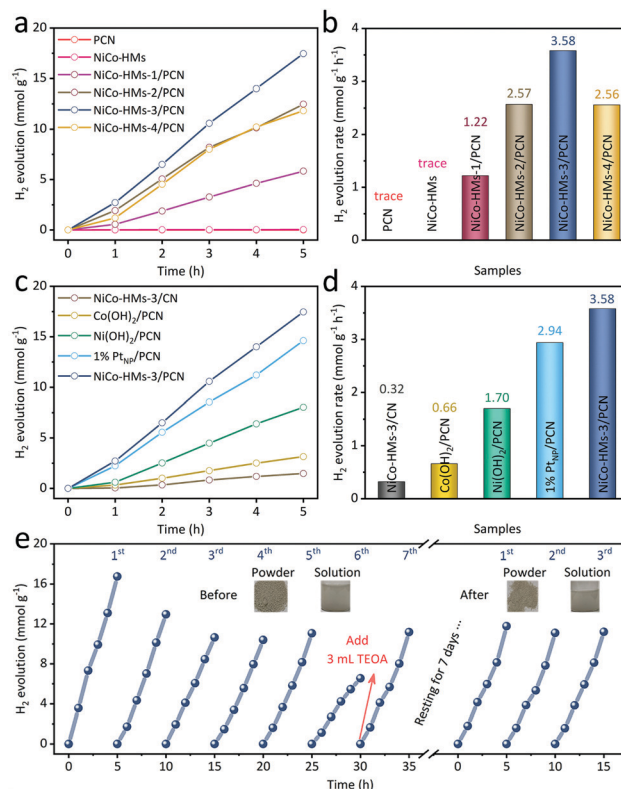

Fig. 2 (a) Time course of H$_2$ evolution and (b) photocatalytic H$_2$-evolution rate over NiCo-HMs/PCN. (c) Time course of H$_2$ evolution and (d) photocatalytic H$_2$-evolution rate over different samples. (e) Photocatalytic stability test of NiCo-HMs-3/PCN.

performance is presented in Table S2 (ESI†), reflecting the superiority of NiCo-HMs cocatalyst in this work.

In addition, the protonated bulk g-C$_3$N$_4$ (PBCN) and protonated tubular g-C$_3$N$_4$ (PTCN) are also fabricated for comparison, and then *in situ* coupled with the NiCo-HM cocatalyst to form the NiCo-HMs-3/PBCN (Fig. S8, ESI†) and NiCo-HMs-3/PTCN (Fig. S9, ESI†). The H$_2$ generation rates of NiCo-HMs-3/PBCN and NiCo-HMs-3/PTCN are 2.14 and 2.98 mmol g^{-1} h^{-1}, respectively, which were considerably lower than that of NiCo-HMs-3/PCN (Fig. S10, ESI†). Surprisingly, the apparent quantum efficiency (AQE) of NiCo-HMs-3 reached 7.9% (Fig. S11, ESI†). These results indicate that a larger contact surface can be realized in the 2D/2D interface formed between the NiCo-HMs and PCN, which contributes to the faster separation and transfer of photoinduced carriers. The Ni–Co layered double hydroxides (NiCo-LDHs) with multilayer structures were prepared for further comparison (Fig. S12 and S13, ESI†). As expected, the H$_2$ evolution rate of NiCo-LDHs-3/PCN (1.48 mmol g^{-1} h^{-1}) is much lower than that of Nico-LDHS-3/PCN under the same conditions (Fig. S14, ESI†).

As revealed in Fig. 2e of continuous cycle experiments for NiCo-HMs-3/PCN, no significant deterioration in photocatalytic activity was observed in successive tests. After 7 cycles, the photocatalytic performance remains the same even after exposing the reaction solution to photocatalysts for 7 days. Furthermore, there are no significant changes in the XPS results of Ni 2p and Co 2p for the spent sample (Fig. S15 and Table S3, ESI†). Similarly, the XRD, FT-IR spectra (Fig. S16, ESI†) and TEM image (Fig. S17, ESI†) of the recycling sample remained nearly constant with a fresh sample, suggesting structural and chemical stability of NiCo-HMs-3/PCN under a photocatalytic process.

The optical absorption properties of PCN and various composite samples are characterized by ultraviolet-visible (UV-vis) absorption spectroscopy (Fig. S18 and S19a, ESI†). It can be observed that the integration of NiCo-HMs contributes to broadening the optical absorption range of PCN with significantly increased absorption in the visible-light region. The Mott–Schottky curves were also plotted (Fig. S19b, ESI†). The flat-band potential of PCN of −0.66 V (*vs.* Ag/AgCl, pH = 6.8) is higher than that of NiCo-HMs (−0.55 V). The corresponding band structure and charge transfer diagram of the NiCo-HMs-3/PCN hybrids are illustrated in Fig. S19d (ESI†).[17] In addition, the N$_2$ adsorption–desorption isotherms of the obtained samples also suggest that a rise in the specific surface area, as well as the pore size range of the NiCo-HMs-3/PCN, also plays a positive role in offering more reactive sites for the HER (Fig. S20, ESI†).

In Fig. 3a, NiCo-HMs-3/PCN indicates a significantly reduced steady-state fluorescence intensity, implying a suppression of photo-generated carrier recombination.[18] The transport and quenching mechanism of photogenerated carriers was further investigated using time-resolved photoluminescence (TR-PL) spectroscopy (Fig. 3b). NiCo-HMs-3/PCN exhibits a considerably shorter average fluorescence lifetime (0.49 ns) than PCN (2.61 ns). Moreover, Fig. S21 (ESI†) depicts the three positive decay components τ_1, τ_2, and τ_3 of NiCo-HMs-3/PCN. In general, τ_1, τ_2 and τ_3 represent the descending rates of photogenerated electrons from the σ^*, π^*, and intermediate trap states to the ground state.[19] Meaningfully, the
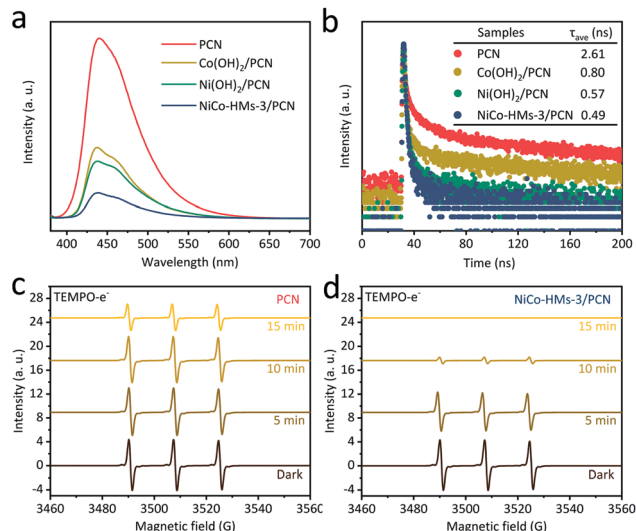

Fig. 3 (a) The steady-state PL spectra and (b) TR-PL spectroscopy of prepared samples. The TEMPO-e$^-$ EPR signals of (c) PCN and (d) NiCo-HMs-3/PCN.

NiCo-HMs-3/PCN presents a higher fraction of the τ_2 component, implying that coupling NiCo-HMs with PCN primarily promotes the excitation of π^* electrons.[20] The shortest lifetime of NiCo-HMs-3/PCN proves the optimal separation efficiency of photogenerated carriers in NiCo-HMs-3/PCN,[21] which explained the reason for the highest H$_2$ generation over the NiCo-HMs-3/PCN sample.

The contact angles of PCN and NiCo-HMs-3/PCN samples with water were captured to identify the hydrophilicity of prepared photocatalysts (Fig. S22, ESI†). The smaller contact angle of NiCo-HMs-3/PCN indicates that the hydrophilicity of PCN is improved by the addition of NiCo-HMs, which facilitates the photocatalytic process in an aqueous solution. Further-more, the electron paramagnetic resonance (EPR) experiments also show outstanding charge transport capacity for NiCo-HMs-3/PCN. Throughout our evaluations of four time periods, both PCN and NiCo-HMs-3/PCN reveal three rapid 1 : 1 : 1 signals for PCN (Fig. 3c), while no signal can be observed for the NiCo-HMs-3/PCN (Fig. 3d), indicating a signal *via* the binding of TEMPO-e$^-$. After 15 min, there was a slight decrease in the EPR signal intensity of PCN, suggesting that a faster carrier transfer channel existed in the NiCo-HMs-3/PCN and more useful electrons for HER are generated.[22]

Furthermore, the photocurrent response (Fig. S23, ESI†) shows a significant increase in the current in the presence of light irradiation. The order of current intensity induced by photogenerated carriers under 80 W LED light (420 nm) irra-diation is NiCo-HMs-3/PCN > Ni(OH)$_2$/PCN > Co(OH)$_2$/PCN > PCN, indicating that NiCo-HMs can effectively promote the separation of photogenerated carriers.[23] Fig. S24 (ESI†) depicts the electrochemical impedance spectra (EIS) of different sam-ples, and the corresponding equivalent circuit is shown in Fig. S25 (ESI†), including the parameter values and their errors. Meaningfully, the NiCo-HMs-3/PCN exhibits a substantially lower R_{ct} value (0.89 kΩ) than those of other samples,
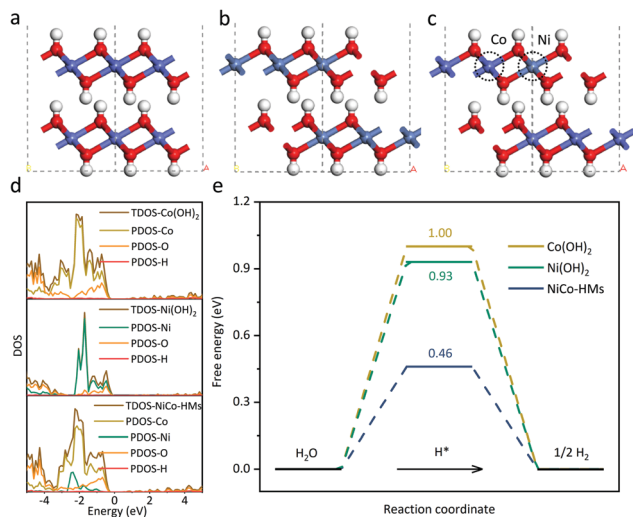
Fig. 4 The optimal geometry models of (a) Co(OH)$_2$, (b) Ni(OH)$_2$ and (c) NiCo-HMs. (d) The calculated density of state (DOS) of Co(OH)$_2$, Ni(OH)$_2$ and NiCo-HMs. (e) The adsorption energies of H*.

demonstrating an ultrafast Faraday process and a good HER kinetics for NiCo-HMs-3/PCN.[24]

Density functional theory (DFT) calculations were adopted to acquire a deeper understanding of the function of NiCo-HMs for enhancing the photocatalytic HER activity. The crystal structures of Co(OH)$_2$, Ni(OH)$_2$ and NiCo-HMs are presented in Fig. 4a–c. From the calculated atomic partial density of states (PDOS) curves, it is observed that the band gaps of Co(OH)$_2$, Ni(OH)$_2$ and NiCo-HMs are 0.555, 0.564 and 0.460 eV, respectively (Fig. 4d). The coexistence of the Ni and Co atoms with strong electronic coupling in the crystal structure decreases the band gap when compared with Co(OH)$_2$ and Ni(OH)$_2$, indicating that the electron transfer in the NiCo-HMs is easier due to the narrower energy band gap. Meanwhile, an increase in the total density of states (TDOS) at the valence band maximum is also found.[25] To confirm that NiCo-HMs could be employed as active sites for the HER, we used DFT to assess the H atom (H*) adsorption capacity on the surface of the Co(OH)$_2$, Ni(OH)$_2$, and NiCo-HM cocatalysts.

Fig. 4e shows that the NiCo-HMs present the lowest H* adsorption energy of 0.46 eV when compared with that of Co(OH)$_2$ (1.00 eV) and Ni(OH)$_2$ (0.93 eV), which indicates that NiCo-HMs as cocatalysts can optimize the HER kinetics.[26] According to the above results, the addition of NiCo-HMs, as a promising cocatalyst with high metallic properties and low H* absorption ability, can effectively settle the disadvantage of high photogenerated carrier recombination for PCN, and thereby enhance the photocatalytic H$_2$ evolution rate. Herein, we propose a probable photocatalytic mechanism by NiCo-HMs/PCN, as revealed in Scheme S1 (ESI†).

In summary, a Ni–Co hydroxide monolayer cocatalyst was developed in this work. The introduction of 2D NiCo-HMs over the 2D PCN was in favour of enhancing the visible light absorption, expanding the interface of electron migration, promoting the separation of photogenerated carriers, and offering synergistic Co–Ni active sites for photocatalytic HER. Furthermore, the lower H* adsorption energy of NiCo-HMs

cocatalyst would improve the HER kinetics, leading to an excellent photocatalytic H$_2$ evolution performance by NiCo-HMs/PCN. This work provides a new vision for the development of low-cost and efficient 2D monolayers with bimetallic active sites as cocatalysts in the HER.

Conflicts of interest

There are no conflicts to declare.

Notes and references

1 Y. Yu, W. Yan, X. Wang, P. Li, W. Gao, H. Zou, S. Wu and K. Ding, *Adv. Mater.*, 2018, **30**, 1705060.
2 F. Mei, Z. Li, K. Dai, J. Zhang and C. Liang, *Chin. J. Catal.*, 2020, **41**, 41–49.
3 X.-P. Yin, S.-W. Luo, S.-F. Tang, X.-L. Lu and T.-B. Lu, *Chin. J. Catal.*, 2021, **42**, 1379–1386.
4 Q. Zhu, Z. Xu, B. Qiu, M. Xing and J. Zhang, *Small*, 2021, **17**, 2101070.
5 H. Yang, A. L. Meng, L.-N. Yang and Z.-J. Li, *Chem. Eng. J.*, 2022, **432**, 134371.
6 Y. Zhang, B. Cui, C. Zhao, H. Lin and J. Li, *Phys. Chem. Chem. Phys.*, 2013, **15**, 7363–7369.
7 M. Zhang, C. Lai, B. Li, F. Xu, D. Huang, S. Liu, L. Qin, X. Liu, H. Yi, Y. Fu, L. Li, N. An and L. Chen, *Chem. Eng. J.*, 2021, **422**, 130120.
8 H. Sakamoto, J. Imai, Y. Shiraishi, S. Tanaka, S. Ichikawa and T. Hirai, *ACS Catal.*, 2017, **7**, 5194–5201.
9 T. Dong, X. Zhang, M. Li, P. Wang and P. Yang, *Inorg. Chem. Front.*, 2018, **5**, 3033–3041.
10 M. Zhang, Z. Luo, M. Zhou, G. Zhang, K. A. Alamry, L. A. Taib, A. M. Asiri and X. Wang, *Appl. Catal., B*, 2017, **210**, 454–461.
11 A. L. Luna, D. Dragoe, K. Wang, P. Beaunier, E. Kowalska, B. Ohtani, D. Bahena Uribe, M. A. Valenzuela, H. Remita and C. Colbeau-Justin, *J. Phys. Chem. C*, 2017, **121**, 14302–14311.
12 Q. Zhu, B. Qiu, H. Duan, Y. Gong, Z. Qin, B. Shen, M. Xing and J. Zhang, *Appl. Catal., B*, 2019, **259**, 118078.
13 Y. Su, X. Xu, R. Li, X. Luo, H. Yao, S. Fang, K. P. Homewood, Z. Huang, Y. Gao and X. Chen, *Chem. Eng. J.*, 2022, **429**, 132241.
14 X. Liu, Y. Zhao, X. Yang, Q. Liu, X. Yu, Y. Li, H. Tang and T. Zhang, *Appl. Catal., B*, 2020, **275**, 119144.
15 J. Kang, X. Qiu, Q. Hu, J. Zhong, X. Gao, R. Huang, C. Wan, L.-M. Liu, X. Duan and L. Guo, *Nat. Catal.*, 2021, **4**, 1050–1058.
16 X. Han, W. Zhang, X. Ma, C. Zhong, N. Zhao, W. Hu and Y. Deng, *Adv. Mater.*, 2019, **31**, 1808281.
17 H. Wang, W. Zheng, W. Li, F. Tian, S. Kuang, Y. Bu and J.-P. Ao, *Appl. Catal., B*, 2017, **217**, 523–529.
18 D. Gao, J. Xu, L. Wang, B. Zhu, H. Yu and J. Yu, *Adv. Mater.*, 2021, **34**, 2108475.
19 P. Kumar, E. Vahidzadeh, U. K. Thakur, P. Kar, K. M. Alam, A. Goswami, N. Mahdi, K. Cui, G. M. Bernard, V. K. Michaelis and K. Shankar, *J. Am. Chem. Soc.*, 2019, **141**, 5415–5436.
20 B. Wu, L. Zhang, B. Jiang, Q. Li, C. Tian, Y. Xie, W. Li and H. Fu, *Angew. Chem., Int. Ed.*, 2021, **60**, 4815–4822.
21 X. H. Jiang, L. S. Zhang, H. Y. Liu, D. S. Wu, F. Y. Wu, L. Tian, L. L. Liu, J. P. Zou, S. L. Luo and B. B. Chen, *Angew. Chem., Int. Ed.*, 2020, **59**, 23112–23116.
22 Q. Liu, J. Shen, X. Yu, X. Yang, W. Liu, J. Yang, H. Tang, H. Xu, H. Li, Y. Li and J. Xu, *Appl. Catal., B*, 2019, **248**, 84–94.
23 X. Yu, H. Su, J. Zou, Q. Liu, L. Wang and H. Tang, *Chin. J. Catal.*, 2022, **43**, 421–432.
24 D. Wang, H. Li, N. Du, Z. Lang, T. Hu and W. Hou, *J. Colloid Interface Sci.*, 2019, **541**, 183–191.
25 H. Zhang, P. An, W. Zhou, B. Guan, P. Zhang, J. Dong and X. Lou, *Sci. Adv.*, 2018, **4**, eaao6657.
26 C. Du, B. Yan and G. Yang, *Nano Energy*, 2020, **76**, 105031.